Chemical Geology 727 (2027) 123802

Contents lists available at ScienceDirect

Chemical Geology

journal homepage: www.elsevier.com/locate/chemgeo

A two-population lattice strain model for H^+-coupled REE incorporation in zircon: calibration, detection threshold, and implications for LREE anomalies

Ioan V. Sanislav [a,*], Mabrouk Sami [b,c]

[a] Economic Geology Research Centre (EGRU), College of Science and Engineering, James Cook University, Townsville, QLD, Australia
[b] Geosciences Department, College of Science, United Arab Emirates University, Al Ain, United Arab Emirates
[c] Geology Department, Faculty of Science, Minia University, El-Minia 61519, Egypt

ARTICLE INFO

Editor: Marco Fiorentini

Keywords:
Zircon
Lattice strain model
Rare earth elements
Water
Defect sites
Partition coefficients
LREE anomalies

ABSTRACT

The classical single-site lattice strain model fails systematically for light and middle rare earth elements (LREE and MREE) in zircons from hydrous, phosphorus-undersaturated magmatic systems, predicting concentrations one to three orders of magnitude below observed values. We develop a two-population model in which the bulk partition coefficient is the mole-fraction-weighted sum of contributions from the ideal ZrO_8 site and a second, enlarged site generated by REE^{3+}–H^+ coupled substitution. Both sites are parameterised by independent Brice parabolas; the fractional occupancy of the defect site, f_d, follows a Langmuir saturation function of water content with half-saturation constant $H_0 = 422$ ppm. Initial calibration of defect-site parameters against the 32 published SIMS spot analyses of Vema Fracture Zone oceanic gabbro zircons reported by De Hoog et al. (2014) gives an unconstrained Nd/Lu optimum of $r_0^{REE-H} = 0.9916$ Å, $E_{REE-H} = 592.1$ GPa, $D_0^{REE-H} = 344.5$ (RMSE = 0.154 $\log_{10}$ units), whereas physically constrained weighted global optimisation, within-grain REE-pattern inversion, and DFT-consistent modest site expansion together indicate a preferred effective defect radius near 0.984 Å with an admissible envelope of ~0.975–0.993 Å. Forward modelling defines a detection threshold in temperature–$[H_2O]$ space below which the defect-site signal is unresolvable from geological noise, requiring $[H_2O]_{zrc} > \sim$30–80 ppm depending on temperature. The model predicts that in hydrous, P-undersaturated systems the REE^{3+}–H^+ mechanism alone can produce La_{zrc} exceeding 0.1 ppm through genuine lattice incorporation, demonstrating that a fixed La threshold is not a universal inclusion-free criterion but depends on temperature, water content, and melt La concentration. The charge-balance ratio f_d^{CB} = (REY–P)/REY, recoverable from routine LA-ICP-MS data without water measurement, provides an independent estimate of defect-site occupancy and correlates with water-based estimates where the REE^{3+}–H^+ mechanism is active, thereby providing a quantitative test of mechanism activation across natural systems. The model is applicable specifically to P-undersaturated, hydrous, low-temperature magmatic systems where the REE^{3+}–H^+ mechanism has been independently confirmed by FTIR spectroscopy and charge-balance analysis.

1. Introduction

Zircon ($ZrSiO_4$) is among the most widely analysed accessory minerals in igneous and metamorphic petrology. Its chemical durability, capacity for nanometre-scale compositional zoning, and suitability for U—Pb geochronology make it a versatile archive of magmatic processes (Watson and Harrison, 1983; Hoskin and Schaltegger, 2003). The theoretical framework underpinning quantitative interpretation of zircon trace element data is the lattice strain model of Brice (1975), formalised for mineral–melt systems by Blundy and Wood (1994). In this formulation, the partition coefficient of a trace element varies with the elastic strain energy generated when the substituting ion deviates in radius from the optimal radius of the crystallographic site, producing a near-parabolic dependence of log *D* on ionic radius. Applied to the eight-fold coordinated Zr^{4+} site, the model successfully predicts HREE and HFSE partitioning (Fig. 1a) and underpins Ce/Ce* oxybarometry (Trail et al., 2012).

Despite this success, the single-site model consistently underpredicts

* Corresponding author.
E-mail address: ioan.sanislav@jcu.edu.au (I.V. Sanislav).

https://doi.org/10.1016/j.chemgeo.2026.123802
Received 25 March 2026; Received in revised form 30 October 2026; Accepted 31 October 2026
Available online 2 November 2026
0009-2541/© 2026 The Authors. Published by Elsevier B.V. This is an open access article under the CC BY license (http://creativecommons.org/licenses/by/4.0/).

LREE and MREE concentrations in zircons from hydrous, phosphorus-undersaturated magmatic systems. Zircons from such systems show Nd/Lu ratios substantially higher than single-parabola predictions anchored to the HREE (De Hoog et al., 2014; Burnham and Berry, 2012). The discrepancy is systematic, largest for the lightest REE, and correlates with the water content of the host system (Fig. 1b) - strongly implying a second incorporation mechanism.

That mechanism is the coupled REE^{3+}–H^{+} substitution, in which a trivalent cation and a proton jointly replace a Zr^{4+} ion, maintaining local charge balance: $REE^{3+} + H^{+} \rightarrow Zr^{4+}$. Three independent lines of evidence support this mechanism: (i) characteristic OH absorption bands near 3100 cm^{-1} in hydrous zircons scale with REE content and are reproduced by DFT calculations of the REE–OH defect geometry (Trail et al., 2011; Balan et al., 2013); (ii) a near-unity molar ratio (H + P)/(REY) in P-undersaturated natural zircons establishes H^{+} as the dominant charge-balance mechanism for excess REE^{3+} (De Hoog et al., 2014); and (iii) within single zircon grains, Nd/Lu and [H_2O] covary systematically across sector zones while HREE ratios remain flat, providing causal evidence that the signal is water-driven rather than a temperature or bulk-composition effect (De Hoog et al., 2014).

Elevated LREE in natural zircon can, however, arise from three distinct causes: (1) the REE^{3+}–H^{+} mechanism described above; (2) xenotime-type substitution ($REE^{3+} + P^{5+} \rightarrow Zr^{4+} + Si^{4+}$), which dominates when $P_{mol} \geq REY_{mol}$; and (3) incorporation of sub-micron inclusions of La-rich phases (monazite, apatite, allanite) during analysis, which Zou et al. (2019) showed is the most likely explanation for La > 0.1 ppm in most published datasets. Distinguishing these three causes requires simultaneous knowledge of P content, H_2O content, and FTIR band attribution - constraints rarely available together. A further, microstructural pathway applies to deformed grains: atom probe tomography shows that crystal-plastic deformation can concentrate incompatible trace elements such as Y, U, Al and Pb along dislocations and dislocation arrays in zircon (Piazolo et al., 2016), producing sub-micron trace-element heterogeneity unrelated to primary growth. The present model accordingly applies to undeformed magmatic zircon, in which such redistribution is absent.

Here we develop a physically grounded two-population lattice strain model for the REE^{3+}–H^{+} mechanism, calibrated against the only published natural dataset satisfying all required conditions: the De Hoog et al. (2014) Vema Fracture Zone oceanic gabbro zircons, in which SIMS measurements of [H_2O], P, and a full REE suite are available in the same analytical spot, FTIR confirms that the 3100 cm^{-1} band dominates, and $P_{mol} < REY_{mol}$ throughout. We demonstrate that the model: (i) reproduces the observed Nd/Lu–H_2O covariation with RMSE = 0.154 log_{10} units and no systematic offset; (ii) defines a quantitative detection threshold in temperature–H_2O space; and (iii) independently predicts an upper limit on La incorporation via this mechanism consistent with the Zou et al. (2019) inclusion-free threshold.

An Excel-based implementation of the defect-modified lattice-strain model is provided as Supplementary Material, allowing users to calculate defect-site fraction, predict REE partitioning, and assess model applicability for their own datasets.

2. The two-population lattice strain model

2.1. The classical single-site framework and its failure

The lattice strain model expresses the partition coefficient D_i of a trace element in terms of the elastic strain energy generated by ionic radius mismatch:

$$D_i = D_0 \exp\left\{ -\frac{4\pi N_A E}{RT}\left[\frac{r_0}{2}(r_i - r_0)^2 + \frac{1}{3}(r_i - r_0)^3\right]\right\} \quad (1)$$

where D_0 is the strain-free partition coefficient for an ion of ideal radius r_0, E is the apparent Young's modulus of the substitution site, N_A is Avogadro's number, R is the gas constant, and T is absolute temperature (Blundy and Wood, 1994; Wood and Blundy, 1997). Eq. 1 applies to a series of ions of a single valence; both D_0 and E depend strongly on the charge mismatch between the substituent and the host site, so a separate parabola is required for each cation charge (Blundy and Wood, 1994). In the present model the relevant series is the isovalent REE^{3+} group substituting onto the Zr^{4+} site. Applied to the ZrO_8 dodecahedron, the model reproduces HREE partitioning with high fidelity, with r_0^{REE-P} = 0.9445 Å and E_{REE-P} = 517 GPa established by Streicher et al. (2023) from kernel density estimation across 39 published datasets, and D_0^{REE-P} following the empirical temperature calibration:

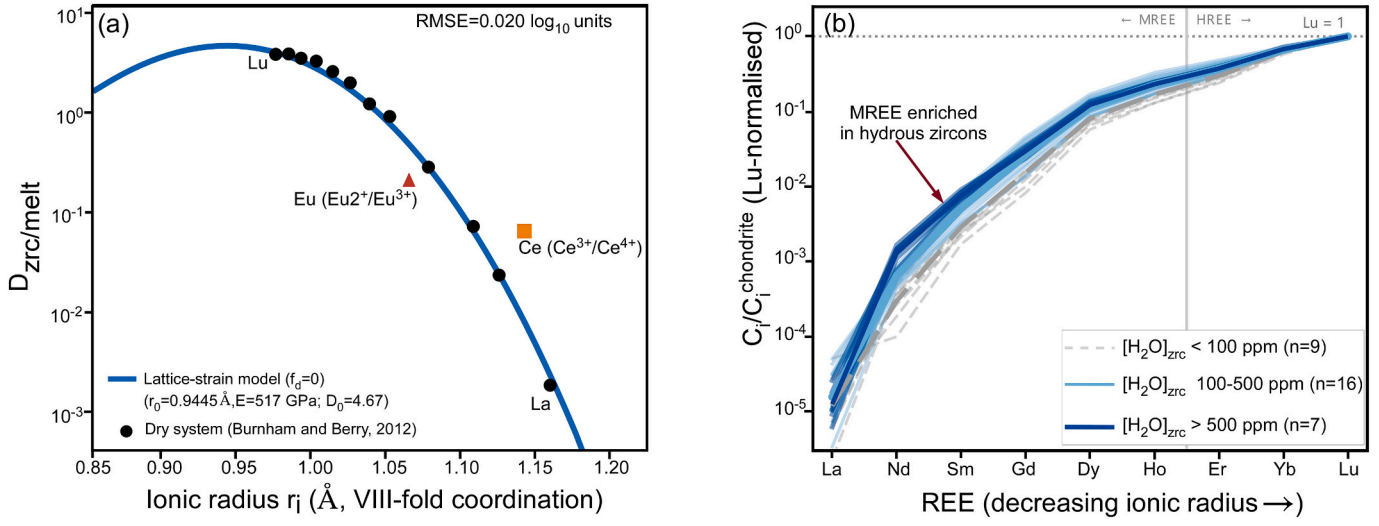


Fig. 1. Failure of the classical single-site lattice strain model for LREE partitioning in zircon. (a) Onuma diagram at T = 1295 °C showing partition coefficients from the dry andesitic melt experiment of Burnham and Berry (2012). All 14 measured REE^{3+} fall on the classical Blundy–Wood parabola (r_0 = 0.9445 Å, E = 517 GPa, D_0 = 4.67; RMSE = 0.020 log_{10} units), confirming that a single lattice site describes partitioning in the absence of water. Ce and Eu are shown separately as mixed-valence elements. (b) REE patterns for De Hoog et al. (2014) Vema gabbro zircons, chondrite-normalised (McDonough and Sun, 1995) and then normalised to Lu (Lu = 1), grouped by [H_2O]zrc. MREE (Nd—Gd) are systematically elevated relative to the HREE with increasing [H_2O], while the heavy-REE (Er—Lu) patterns remain subparallel; La—Pr lie near analytical detection (La/Lu ≈ 10^{-5}). This water-correlated MREE enrichment is the diagnostic signature of the REE^{3+}–H^{+} mechanism and cannot be reproduced by a single Brice parabola.

$$\ln D_0^{REE-P} = \frac{-13594 \pm 1500}{T\,[\mathrm{K}]} - 7.127 \pm 1.309 \quad (2)$$

(Streicher et al., 2023; $R^2 = 0.768$, $n = 39$). These parameters are not free in our model.

The failure of the single-site model for LREE is illustrated by two contrasting datasets. Burnham and Berry (2012) measured partition coefficients for 14 REE in a dry andesitic melt at 1295 °C; La falls on the HREE-anchored parabola with D(La) = 0.002, consistent with the lattice-only prediction (Fig. 1a). Thomas et al. (2002) determined partition coefficients from SIMS analyses of natural melt inclusions in zircon from a hydrous tonalitic melt (~940 °C, 4–9 wt% H_2O); their median D(La) = 0.05, roughly 25 times above the temperature-corrected lattice prediction. Phosphorus is below detection limits in these zircons, ruling out xenotime substitution. The excess must reflect an additional incorporation mechanism active in the hydrous system.

2.2. Two-population partition coefficient

We conceptualise zircon as containing two distinct populations of substitution environments: a P-balanced population on a near-ideal ZrO_8 site (REE^{3+} charge-compensated by P^{5+}), and an H-coupled population on a more strongly expanded site generated by REE^{3+}–H^+ substitution. DFT calculations show that REE incorporation drives mean Zr—O bond elongation, expanding the effective site radius (Balan et al., 2013). The structural consequence is an enlarged site that preferentially accommodates MREE and LREE relative to the P-balanced site.

At thermodynamic equilibrium the bulk partition coefficient is the mole-fraction-weighted average:

$$D_i = (1 - f_d)\cdot D_i^{REE-P} + f_d \cdot D_i^{REE-H} \quad (3)$$

where f_d is the fraction of REE residing on the H-coupled (REE—H) site. Here and throughout, the superscripts "REE–P" and "REE–H" denote the two REE point-defect populations, charge-balanced respectively by P^{5+} (xenotime-type substitution) and by H^+. Both place REE^{3+} on the Zr^{4+} site and deform the host ZrO_8 polyhedron, the REE–H population more strongly. Both D_i^{REE-P} and D_i^{REE-H} follow Eq. (1) with their respective site parameters. The model reduces exactly to the classical single-site formulation when $f_d = 0$.

The sensitivity structure of Eq. (3) is the model's primary diagnostic prediction (Fig. 2a). For LREE (La, $r = 1.160$ Å), $D^{REE-P}(La) \approx 0.004$ at 787 °C - orders of magnitude below D^{REE-P} for HREE. Even a modest defect-site contribution elevates La substantially. For HREE such as Lu ($r = 0.977$ Å), the radius lies near the apex of both the lattice and the defect parabola, so the strain term is small at each site and the defect-to-lattice ratio approaches that of the strain-free prefactors, $D^{REE-H}(Lu)/D^{REE-P}(Lu) \approx D_0^{REE-H}/D_0^{REE-P} \approx 0.17$ (Fig. 2b). Because this ratio is nearly the same for all HREE, which cluster near both apices, increasing f_d scales the HREE together (at $f_d = 0.5$ their bulk partition coefficients fall by ≈ 40% relative to the dry lattice) and leaves HREE/HREE ratios such as Yb/Lu almost unchanged, so Lu acts as a near-invariant denominator. The defect site enhances partitioning only for the LREE and MREE, which lie far from both apices (e.g. $D^{REE-H}(Nd)/D^{REE-P}(Nd) \approx 2.5$), so f_d raises Nd/Lu strongly. This differential sensitivity, LREE–MREE strongly responsive, HREE-internal ratios insensitive, is the signature of the REE^{3+}–H^+ mechanism and underpins Nd/Lu as its primary observable.

The defect-site partition coefficient is described using an analogous lattice strain formulation:

$$D_i^{REE-H} = D_0^{REE-H} \bullet \exp\left\{ -\frac{4\pi N_A E_{REE-H}}{RT}\left[\frac{1}{2} r_0^{REE-H}\left(r_i - r_0^{REE-H}\right)^2 + \frac{1}{3}\left(r_i - r_0^{REE-H}\right)^3\right]\right\} \quad (4)$$

where D_0^{REE-H}, r_0^{REE-H}, and E_{REE-H} are the defect-site analogues of the lattice strain parameters.

Combining Eqs. (1), (3) and (4), the full defect-modified lattice strain model can be written as:

$$D_i = (1 - f_d) D_0^{REE-P} exp\left\{ -\frac{4\pi N_A E_{REE-P}}{RT} \Psi\left(r_i, r_0^{REE-P}\right)\right\} + f_d D_0^{REE-H} exp\left\{ -\frac{4\pi N_A E_{REE-H}}{RT} \Psi\left(r_i, r_0^{REE-H}\right)\right\} \quad (5)$$

where $\Psi(r_i, r_o) = \frac{1}{2} r_0 (r_i - r_o)2 + \frac{1}{3}(r_i - r_o)3$ is the Brice elastic strain term.

2.3. Defect-site parameters

The defect-site Young's modulus is derived from the same Hazen–-Finger polyhedral bulk modulus relationship used for the lattice site (Streicher et al., 2023), which relates E to the site radius:

$$E_{REE-H} = Q \cdot \left(r_O + r_0^{REE-H}\right)^{-3} \quad (6)$$

where $r_O = 1.38$ Å is the ionic radius of oxygen (Shannon, 1976) and $Q = 6489 \pm 27$ GPa Å^3 is calibrated by Streicher et al. (2023). Once r_0^{REE-H} is fixed, Eq. (6) defines a physically constrained estimate of E_{REE-H}. We use this relation in the weighted global optimisation and within-grain pattern-shape inversions below; for comparison, we also report the unconstrained Nd/Lu optimum obtained when E_{REE-H} is fitted directly. This leaves three effective parameters to be calibrated from natural data: r_0^{REE-H}, D_0^{REE-H}, and f_d, with E_{REE-H} either fitted directly or linked to r_0^{REE-H} through Eq. (6).

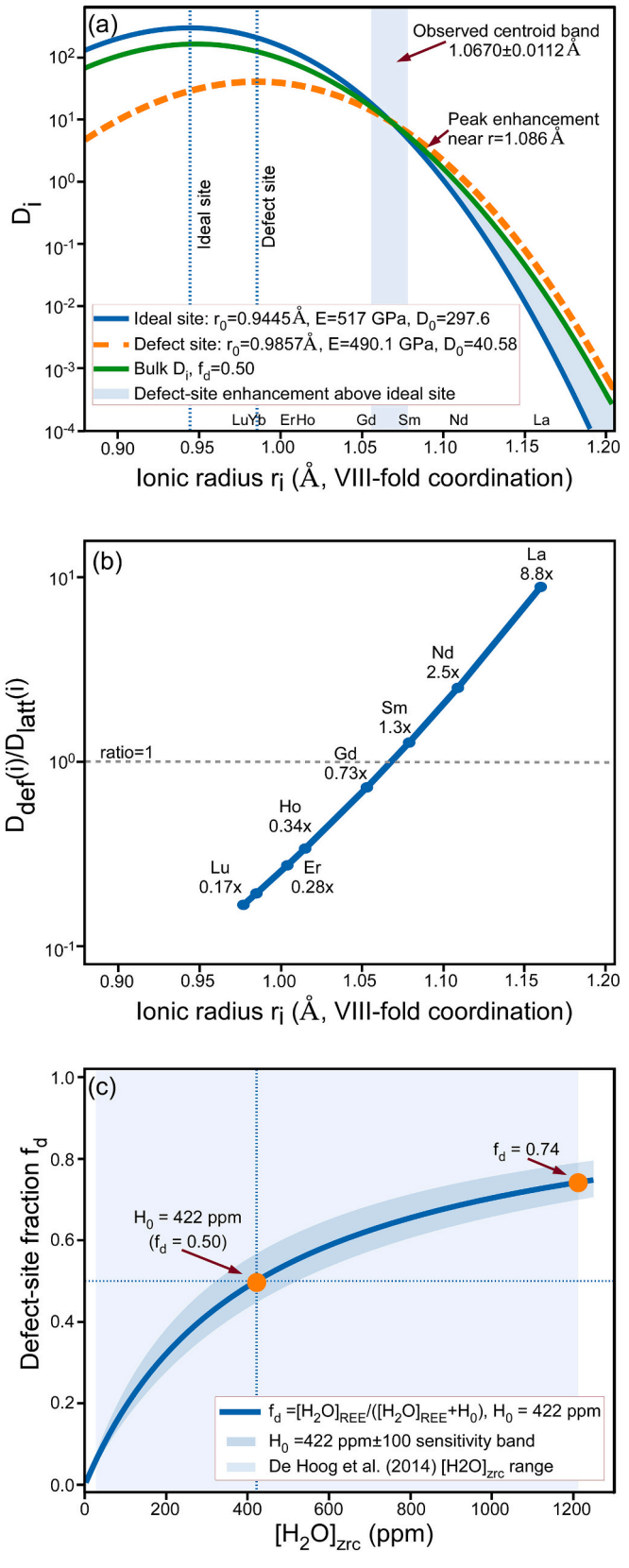
We emphasise that r_0^{REE-H} cannot be derived from published DFT calculations. DFT studies (Balan et al., 2013) compute O—H bond lengths within specific defect geometries, not the Brice optimal radius for the REE^{3+} series at the defect site. The defect-site DFT calculations required to constrain r_0^{REE-H} from first principles – formation energies for all 14 REE at the [REE–O_8/H] site - have not been published. Published DFT bond lengths nevertheless provide a weak geometric prior: they imply only modest expansion of the defect environment relative to the ideal ZrO_8 site, consistent with a small positive shift in effective site radius rather than a large displacement into the extreme LREE domain. In this sense DFT is used here as an independent consistency check on the magnitude of site expansion, not as a direct source of Brice parameters.

2.4. Langmuir occupancy function

The defect fraction f_d must satisfy: $0 \le f_d \le 1$; $f_d \to 0$ as $[H_2O] \to 0$; and f_d should saturate at high $[H_2O]$. Treating defect site creation as a Langmuir equilibrium between ideal and REE–H occupied Zr sites yields:

$$f_d = \frac{[H_2O]_{REE}}{[H_2O]_{REE} + H_0} \quad (7)$$

where $[H_2O]_{REE}$ is the water component coupled to REE^{3+} charge balance (corresponding to the 3100 cm^{-1} FTIR band; De Hoog et al., 2014; Cui et al., 2023), and $H_0 = 422$ ppm is the half-saturation constant, estimated by equating Eq. (7) with the independent charge-balance defect-site fraction (Eq. (8)) for the De Hoog et al. (2014) dataset (Fig. 2c). Both $[H_2O]_{REE}$ and H_0 are expressed as parts per million by weight of equivalent H_2O (wt ppm H_2O), following the FTIR convention of De Hoog et al. (2014) and Trail et al. (2011); because f_d depends only on their ratio, its value is independent of this choice provided the two are expressed in the same units. Because this estimate is weakly constrained (a few hundred ppm) and H_0 trades off with D_0^{REE-H}, we fix $H_0 = 422$ ppm within this range; the calibration and all predictions are invariant to the choice across 200–600 ppm. When only SIMS total $[H_2O]$ is available and FTIR band-specific data are absent, $[H_2O]_{REE}$



(caption on next column)

Fig. 2. Two-population lattice-strain model incorporating defect-mediated REE incorporation. (a) Ideal lattice-site (solid blue), defect-site (dashed red), and bulk partitioning (green; Eq. 5) shown for the preferred physically constrained parameter set at 787 °C and $f_d = 0.50$. Shaded region indicates the observed within-grain centroid of REE-pattern excess (1.067 ± 0.011 Å), demonstrating that defect-related enrichment is centered in MREE radius space and requires only modest expansion of the ZrO_8 site. (b) Ratio $D^{REE–H}/D^{REE–P}$ across the REE series calculated from the same parameter set, showing moderate but systematic enhancement toward larger ionic radii, with strongest amplification for Nd—La and strong suppression of HREE (ratio ≈ 0.17). (c) Langmuir-type defect-site occupancy function (Eq. 7) relating defect fraction f_d to zircon H_2O content, with sensitivity to $H_0 = 422 \pm 100$ ppm and the range of the De Hoog et al. (2014) dataset indicated. The two marked points are the half-saturation point ($f_d = 0.50$, where $[H_2O]_{zrc} = H_0 = 422$ ppm) and the maximum defect-site fraction reached in that dataset ($f_d = 0.74$, at the highest measured $[H_2O]_{zrc} \approx 1212$ ppm); the latter sets the upper bound used for the maximum-La estimate in Section 4.2. (For interpretation of the references to colour in this figure legend, the reader is referred to the web version of this article.) (For interpretation of the references to colour in this figure legend, the reader is referred to the web version of this article.)

should be estimated as $\min([H_2O]_{total}, REY_{mol} - P_{mol})$ on a molar basis, where $REY_{mol} - P_{mol}$ is the charge-balance excess requiring H^+ compensation (De Hoog et al., 2014), with $[H_2O]_{total}$ taken as moles of H^+ (two per H_2O molecule; molar mass 18.015 g mol^{-1}) and one H^+ required per excess REE^{3+}. Where the zircon contains enough P for xenotime-type substitution to balance all the REE ($P_{mol} \geq REY_{mol}$), $[H_2O]_{REE} \approx 0$ and the model predicts no defect-site signal.

Eq. (7) is not an empirical fit but follows from treating the two charge-compensation states of a REE^{3+} ion on the Zr^{4+} site as a local equilibrium. A given REE^{3+} is compensated either without hydrogen – by coupled substitutions such as $P^{5+} \rightleftharpoons Si^{4+}$ (the ideal lattice site of Section 2.2) - or by a proton, through the substitution $REE^{3+} + H^+ \rightleftharpoons Zr^{4+}$ that produces the 3100 cm^{-1} OH band and the near-1:1 trivalent-cation-to-hydrogen correlation observed in synthesis experiments (Trail et al., 2011; De Hoog et al., 2014). Writing the interconversion as $REE_{REE–P} + H^+ + Si^{4+} \rightleftharpoons REE_{REE–H} + P^{5+}$, in which the P^{5+} released from the tetrahedral site is replaced by Si^{4+}, and with the proton supplied from the REE-coupled water reservoir of effective concentration $[H_2O]_{REE}$, mass action gives an equilibrium constant $K = [REE_{REE–H}]/([REE_{REE–P}] \cdot [H_2O]_{REE})$, so that $f_d = K[H_2O]_{REE}/(1 + K[H_2O]_{REE})$ - Eq. (7) with $H_0 = 1/K$. The half-saturation constant H_0 is therefore the inverse of this equilibrium constant - the value of $[H_2O]_{REE}$ at which half of the REE are H-coupled. A saturating (Langmuir) form is required rather than a linear, Henry's-law dependence because the REE population is finite: as water increases, every REE site is eventually proton-compensated, so f_d is bounded by unity and must level off. The treatment assumes local equilibrium and a single equilibrium constant independent of REE loading - that is, dilute, non-interacting sites, which are the standard Langmuir assumptions. Formally this is the same mass-action speciation step used to describe the $H_2O_{melt} + O_{melt} \rightleftharpoons 2OH_{melt}$ equilibrium in silicate melts (Stolper, 1982).

2.5. Charge-balance diagnostic

When FTIR and SIMS H_2O measurements are both unavailable, the charge-balance ratio:

$$f_d^{CB} = \frac{REY_{mol} - P_{mol}}{REY_{mol}} \quad (8)$$

provides an estimate of f_d from routine LA-ICP-MS data alone. This follows directly from the stoichiometry of the REE^{3+}–H^+ mechanism: each H^+ charge-balances one REE^{3+} in excess of what P^{5+} can accommodate via xenotime substitution (De Hoog et al., 2014). When $f_d^{CB} \leq 0$, xenotime substitution is sufficient and the H^+-coupled mechanism is not required. The behaviour of this proxy and its relationship to

independent estimates of f_d are examined in Section 4.3.

It is useful to set Eqs. (7) and (8) within the single mass balance from which both follow. Charge compensation of REE^{3+} on the Zr^{4+} site proceeds either by P^{5+} (the xenotime substitution $REE^{3+} + P^{5+} \rightleftharpoons Zr^{4+} + Si^{4+}$) or by H^+ ($REE^{3+} + H^+ \rightleftharpoons Zr^{4+}$; Section 2.4). The number of H-compensated (defect) REE is therefore the REE in excess of P, but no greater than the available REE-coupled water can support, so the defect fraction is bounded by $f_d \leq \min([H_2O]_{REE}, REY_{mol} - P_{mol})/REY_{mol}$ on a molar basis - $[H]_{zrc}$ and the REE excess are coupled, not independent. The charge-balance ratio of Eq. (8), $(REY_{mol} - P_{mol})/REY_{mol}$, is the water-abundant limit of this expression and hence an upper bound on f_d: it is reached only when REE-coupled water is sufficient to compensate every excess REE. Eq. (7) describes how f_d approaches this ceiling as REE-coupled water increases, in smooth (Langmuir) form with crossover scale H_0 fixed by matching the two on the De Hoog et al. (2014) dataset; because the $[H_2O]_{REE}$ it takes as input is itself capped at $REY_{mol} - P_{mol}$ (Section 2.4), the water-based and charge-balance estimates are not independent. The two therefore correlate and agree near the calibration, but the charge-balance estimate exceeds the water-based one where water is limiting (low $[H_2O]$), as observed in the De Hoog dataset (Section 4.3).

3. Calibration against natural data

3.1. The De Hoog et al. (2014) dataset

De Hoog et al. (2014) measured $[H_2O]$ and a full suite of trace elements by SIMS in 34 spots across nine zircon grains from Fe—Ti oxide gabbros of the Vema Fracture Zone (Mid-Atlantic Ridge, 11°N), part of the Vema Lithospheric Section. The grains span $[H_2O]$ from <25 to 1212 ppm. Two spots (L3 spot 3; XL2 spot 3) lack measured H_2O and are excluded from calibration, leaving 32 usable spots.

The dataset satisfies all required conditions for the REE^{3+}–H^+ mechanism. The molar ratio $(H + P)/REY$ has a median of 1.02, confirming that REE charge balance is achieved jointly by H^+ and P^{5+}. In 31 of 32 spots, $P_{mol} < REY_{mol}$, so the REE excess not accommodated by xenotime substitution ranges from 0 to 97% of total REY. FTIR spectra show a dominant 3100 cm^{-1} band with only a minor 3200 cm^{-1} contribution, consistent with REE^{3+}–H^+ coupling being the principal water incorporation mechanism (De Hoog et al., 2014; Cui et al., 2023).

Across all 32 spots, Nd/Lu ($\times 10^3$) shows a strong positive Spearman correlation with $[H_2O]$ ($r_s = 0.86$, $p < 0.001$). The strongest causal evidence comes from grain L16, which shows a 17-fold decrease in $[H_2O]$ from core (1201 ppm) to rim (70 ppm), accompanied by a 5-fold decrease in Nd/Lu (27.3 to 5.3×10^3), while Yb/Lu changes by less than 10% across the same transect. The within-crystal setting removes inter-grain analytical bias, and the near-constant Yb/Lu points to a stable melt HREE pattern; the covarying Ti-in-zircon temperature is assessed explicitly below. This pattern is systematic across the dataset: in every grain with a core-to-rim transect, both $[H_2O]$ and total REE decrease from core to rim – by up to ~35-fold and ~ 18-fold, respectively – and across all 31 spots $[H_2O]$ correlates strongly with total REE (Spearman $r_s = 0.85$) and Y ($r_s = 0.87$). This coupled depletion is the expected signature of the REE^{3+}–H^+ substitution operating during growth: as the melt REE budget is progressively depleted, the charge-balancing H^+ incorporated into the zircon declines in step. Crucially, the effect is not simple dilution – the MREE/HREE ratio Nd/Lu falls 3- to 5-fold core to rim and correlates strongly with $[H_2O]$ ($r_s = 0.83$), whereas the HREE/HREE ratio Yb/Lu varies only marginally (<15% per transect; $r_s = 0.51$). The water-correlated signal is therefore specific to MREE enrichment, as expected if H^+ availability governs occupancy of the enlarged defect site rather than the bulk REE content. Ti-in-zircon temperature also declines from core to rim, but lattice-strain partitioning across the observed range reproduces only a ~ 2.6-fold variation in Nd/Lu against the ~17-fold range observed; Nd/Lu remains strongly correlated with $[H_2O]$ after controlling for temperature (partial $r_s = 0.77$), whereas the residual correlation with temperature is negligible (partial $r_s = 0.16$). The MREE signal therefore reflects water-controlled defect occupancy, not the covarying temperature.

We stress that this dataset constitutes the calibration set for our model - not an independent validation. The defect-site parameters are fitted to these 32 points. Because De Hoog et al. (2014) did not analyse the melt from which these zircons grew, we do not derive zircon–melt partition coefficients from their data; the calibration observable is instead the intra-zircon ratio Nd/Lu and its covariation with $[H_2O]$. As the Vema zircons are comagmatic, the parental-melt REE pattern is approximately common to all spots and enters this ratio only as a near-constant scaling, so the fitted Nd/Lu variation tracks the water-driven defect fraction f_d rather than melt evolution. The within-grain L16 transect, in which the melt is fixed by construction, confirms the $[H_2O]$–Nd/Lu covariation independently of any melt-composition assumption. Sections 3.2–3.3 characterise the calibration performance and its limitations.

3.2. Calibration of defect-site parameters

We first calibrate r_0^{REE-H}, E_{REE-H}, and D_0^{REE-H} by minimising the root-mean-square error in $\log_{10}$(Nd/Lu) across the 32 spots, with $H_0 = 422$ ppm held fixed at the value estimated in Section 2.4 (independent of the Nd/Lu calibration) and temperature fixed at 787 °C (the mean Ti-in-zircon temperature of the 34 De Hoog et al. (2014) spots, calculated from their reported Ti concentrations using the Ti-in-zircon thermometer of Watson et al. (2006) as recalibrated by Ferry and Watson (2007) with $aTiO_2 = 0.6$ and $aSiO_2 = 1.0$, values appropriate for the ilmenite-bearing, rutile-absent Vema gabbros). The Ti-in-zircon temperatures of these spots span ~700–865 °C rather than a single value; refitting the calibration with spot-specific temperatures leaves the RMSE essentially unchanged (0.154 $\log_{10}$ units) and shifts the defect-site radius by less than its uncertainty, so the fixed-temperature approximation does not bias the result. Initial values of r_0^{REE-H} were guided by DFT estimates of Zr—O bond elongation in the REE^{3+}–H^+ defect environment (Balan et al., 2013), which constrain r_0^{REE-H} to be modestly larger than r_0^{REE-P}. The unconstrained Nd/Lu optimum is:

$$r_0^{REE-H} = 0.9916\ \text{Å}, E_{REE-H} = 592.1\ \text{GPa}, D_0^{REE-H} = 344.5$$

For comparison, the ideal lattice site has $r_0^{REE-P} = 0.9445$ Å, $E_{REE-P} = 517$ GPa and $D_0^{REE-P} = 297.6$ at 787 °C; the defect-site optimum thus represents only a modest expansion in optimal radius (≈0.05 Å). These give RMSE = 0.154 $\log_{10}$ units across 32 spots (Fig. 3), with no systematic offset between predicted and observed Nd/Lu. All parameter values used in this study are collected in Table S1.

The unconstrained optimum places the defect-site parabola peak close to the MREE (around Ho) and reproduces the observed Nd/Lu–H_2O covariation with no systematic offset. Nd/Lu is adopted as the calibration observable rather than a La- or Ce-based ratio because La, Ce and Pr occur at low concentrations in zircon and are the most susceptible to inclusion contamination and analytical uncertainty, whereas Nd and Lu are analytically robust (see Section 5.3). However, Nd/Lu alone primarily constrains enrichment amplitude, not the detailed position of the defect parabola. When the weighted global optimisation, Lu-normalised within-grain ratio-of-ratios, peak-position proxy, and DFT-consistent modest site expansion are considered together, the preferred effective defect radius shifts slightly lower to ~0.984 Å, with an admissible envelope of approximately 0.975–0.993 Å. The strongest geometric signal in the De Hoog dataset is an MREE-centred enrichment in the Nd–Sm–Gd region rather than the extreme La tail. The resulting lattice-strain and defect-site parameters, including unconstrained and physically constrained solutions, are summarized in Table S1. Parameter values in Table S1 were obtained by direct forward modelling and grid search minimization of Nd/Lu misfit, with additional constraints imposed by REE pattern shape and peak position.

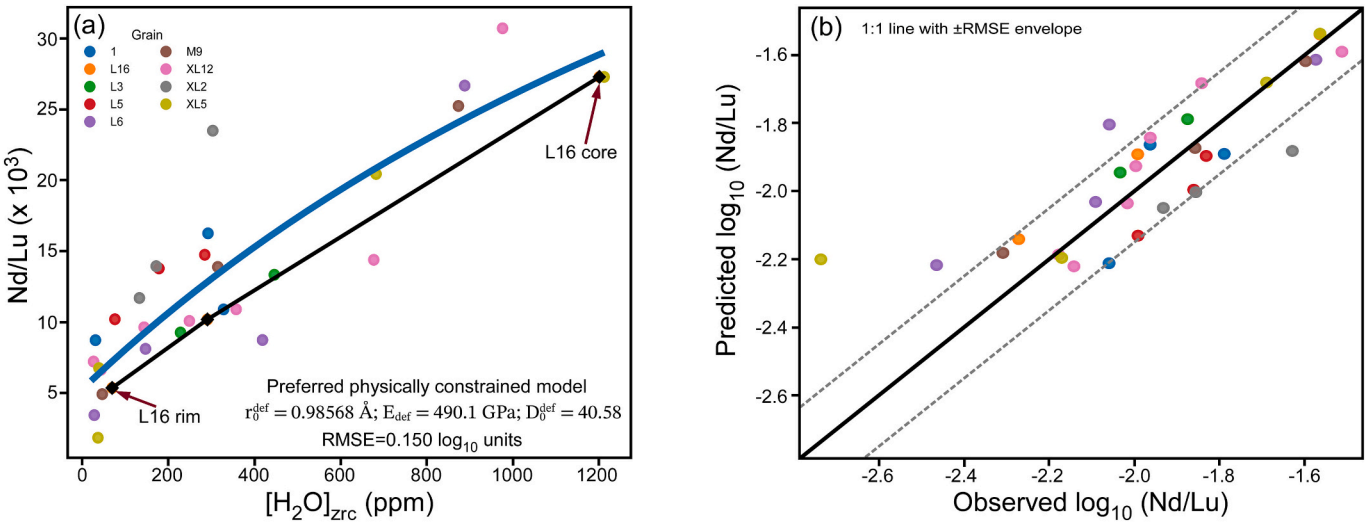


Fig. 3. Calibration of the two-population model against the De Hoog et al. (2014) dataset (32 spots, 9 grains, $T = 787$ °C). Symbols are coloured by grain. (a) Nd/Lu ($\times 10^3$) vs $[H_2O]_{zrc}$ (ppm). The solid blue curve shows a physically constrained solution ($r_0^{REE-H} = 0.98568$ Å, $E_{REE-H} = 490.1$ GPa, $D_0^{REE-H} = 40.58$) consistent with the integrated estimate ($r_0^{REE-H} = 0.984$ Å; Table S1). Grain L16 is highlighted with a diamond symbol; the arrow traces its core-to-rim trajectory (core: $[H_2O] = 1201$ ppm, Nd/Lu = 27.3×10^3; rim: $[H_2O] = 70$ ppm, Nd/Lu = 5.3×10^3), constituting within-grain evidence for the mechanism. The model reproduces the first-order increase of Nd/Lu with water content with RMSE = 0.150 $\log_{10}$ units. (b) Predicted vs observed $\log_{10}$(Nd/Lu) on 1:1 axes with ±RMSE band. No systematic offset is present. (For interpretation of the references to colour in this figure legend, the reader is referred to the web version of this article.) (For interpretation of the references to colour in this figure legend, the reader is referred to the web version of this article.)

3.3. Parameter uncertainty and LREE prediction reliability

The calibration problem is partially non-unique because r_0^{REE-H} and E_{REE-H} both influence the curvature and position of the defect parabola. Nd/Lu robustly captures the existence and magnitude of defect-related enrichment, but it under-resolves the position of the parabola peak if used alone. Lu-normalised ratio-of-ratios and within-grain differential REE patterns carry additional geometric information because they respond to curvature across the Nd–Sm–Gd–Dy segment of the spectrum.

The unconstrained Nd/Lu-only fit gives a broad Hessian-based 95% interval of [0.933, 1.051] Å, but this overstates the standalone uncertainty on site geometry because r_0^{REE-H} and E_{REE-H} trade off against each other in the fit: a wide range of (r_0, E) combinations reproduces the Nd/Lu data almost equally well, so the radius appears poorly constrained only because E is left free. Under the physically constrained E(r_0) relation, weighted global optimisation and within-grain pattern-shape inversion narrow the admissible range to ~0.975–0.993 Å and favour an effective radius near 0.984 Å. LREE predictions therefore remain more uncertain than Nd/Lu or the general MREE shape, but the present dataset does constrain the defect-related enrichment to a modestly enlarged, MREE-centred site rather than an arbitrary broad LREE-facing parabola. Table S1 further documents the admissible parameter space and illustrates how covariance between r_0^{REE-H} and E_{REE-H} is reduced by incorporating physical constraints and REE pattern shape information.

For Nd ($r = 1.109$ Å), which is only 0.17 Å from r_0^{REE-H}, the uncertainty is much smaller and Nd/Lu predictions are robust. The model's reliable observables are thus Nd/Lu and the general MREE shape, not absolute LREE concentrations.

4. Model predictions

4.1. Detection threshold in temperature–H_2O space

To map the conditions under which the REE^{3+}–H^+ mechanism leaves a resolvable imprint on the zircon REE pattern, we compare the signal it produces in Nd/Lu against the natural scatter in that ratio. The signal is the predicted enrichment of Nd/Lu relative to the mechanism-free ($f_d = 0$) baseline:

$$\text{Signal} = \log_{10}\left(\frac{Nd/Lu_{wet}}{Nd/Lu_{dry}}\right) \quad (9)$$

where Nd/Lu_{wet} is the model prediction at a given $[H_2O]$ and temperature, and Nd/Lu_{dry} is the lattice-site-only baseline ($f_d = 0$). We define the detection threshold as the minimum $[H_2O]$ at which the signal exceeds twice the root-mean-square geological noise estimated from scatter in the De Hoog calibration ($\sigma = 0.20$ $\log_{10}$ units, taken conservatively to avoid circularity with the noise estimate from calibration residuals).

Fig. 4 shows the signal as a filled contour map in temperature–$[H_2O]$ space, with the 2σ detection boundary as a dashed curve. Two published systems are plotted:

- De Hoog et al. (2014): 787 °C, $[H_2O]_{zrc}$ up to 1212 ppm → well above threshold.
- Thomas et al. (2002): ~940 °C, melt H_2O = 4–9 wt% → above threshold, but zircon H_2O unmeasured and REE scatter large (IQR ~1 order of magnitude per element), preventing f_d recovery -signal present, unresolvable.

The detection threshold maps the specific conditions under which Nd/Lu can serve as a proxy for f_d. Systems above the boundary have a measurable defect-site signal; those below do not. This quantitative boundary was not previously available and provides clear applicability criteria for the model.

A counterintuitive feature of the map is that the signal increases with temperature at fixed $[H_2O]$. This occurs because the exponential strain term in Eq. 1 scales as E/T, so a higher temperature reduces the strain penalty; since Nd lies much farther from r_0^{REE-P} than Lu, the reduction is larger for Nd, raising D^{REE-P}(Nd) relative to D^{REE-P}(Lu) and elevating the dry baseline Nd/Lu (the prefactor D_0^{REE-P} cancels in this ratio). At the same time D_0^{REE-P} decreases with temperature (Eq. 2) toward D_0^{REE-H}, which we hold temperature-independent because the defect site is calibrated at a single temperature (787 °C); since the Nd/Lu signal is governed mainly by the strain term, this assumption has only a secondary effect on the detection map. The defect site becomes relatively more competitive and D^{REE-P}(Lu) approaches D^{REE-H}(Lu). The relative

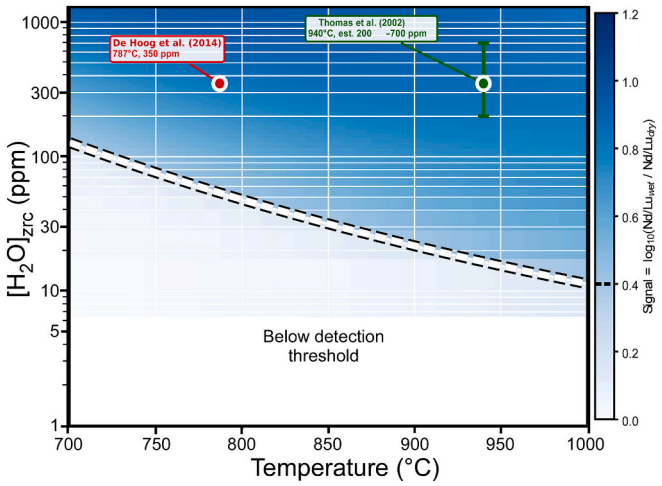


Fig. 4. Detection threshold in temperature–$[H_2O]_{zrc}$ space where [H2O]zrc denotes the REE-coupled (REE^{3+}-charge-balancing) water and excludes vacancy-related hydroxyl. The filled colour map shows signal = $\log_{10}(Nd/Lu_{wet}$ / $Nd/Lu_{dry})$ predicted by the two-population model across the relevant T–$[H_2O]$ range. The dashed black curve marks the 2σ detection boundary (signal = 0.40 $\log_{10}$ units, based on observed scatter σ = 0.20). Two published systems are plotted at their estimated conditions: De Hoog et al. (2014) (787 °C, 350 ppm mean; measured [H2O]$_{zrc}$, above threshold); Thomas et al. (2002) (940 °C, 200–700 ppm estimated from melt H_2O partition; above threshold but f_d unresolvable due to absent zircon $[H_2O]$ measurement). Both systems fall where the model predicts.

defect-site enhancement of Nd/Lu therefore grows at higher T, making the signal easier to detect - but only if $[H_2O]_{zrc}$ is sufficient.

4.2. Upper limit on La incorporation via H+-coupled substitution

The model predicts D_{tot}(La) as a function of f_d and temperature:

$$D_{tot}(La) = (1 - f_d)D_{REE-P}(La) + f_d D_{REE-H}(La) \quad (10)$$

At 787 °C the model predicts a strong increase in D_{tot}(La) with increasing defect-site fraction, while the lattice-only baseline remains low. Because D_{tot}(La) is linearly mixed between lattice and defect contributions, even modest f_d values produce order-of-magnitude increases

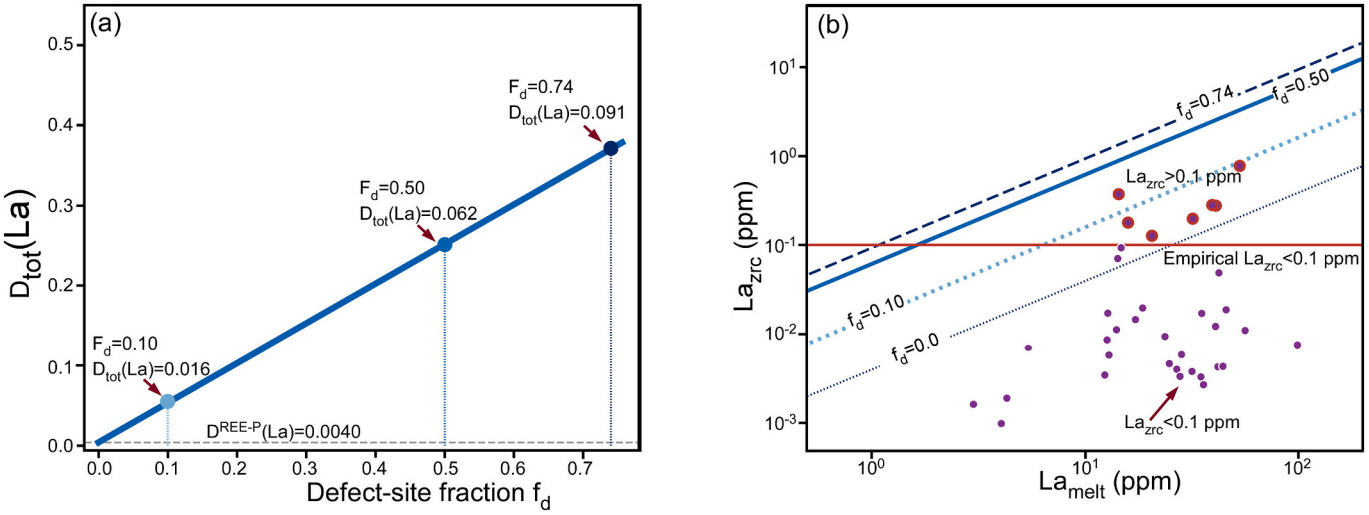


Fig. 5. Defect-mediated enhancement of La incorporation in zircon and implications for the Zou et al. (2019) threshold. (a) Total La partition coefficient (D_{tot}(La)) as a function of defect-site fraction (f_d), showing linear mixing between the lattice endmembers ($D^{REE-P} \approx 0.004$, at $f_d = 0$) and the pure defect-site endmember ($D^{REE-H} \sim 0.121$, the $f_d = 1$ limit). Over the calibrated range ($f_d \leq 0.74$) D_{tot}(La) rises from 0.004 to 0.090 - roughly four-fold by $f_d \approx 0.1$, and more than an order of magnitude (~23× the lattice value) at the maximum $f_d \approx 0.74$ implied by the calibration dataset demonstrating the sensitivity of LREE partitioning to minor structural modification of zircon. (b) Zircon La concentration (La_{zrc}) as a function of melt La concentration (La_{melt}). Model trajectories are shown for $f_d = 0$, 0.10, 0.50 and 0.74 ($La_{zrc} = D_{tot}(La) \times La_{melt}$); the $f_d = 0$ line is the dry, lattice-controlled baseline ($La_{zrc} = D^{REE-P}(La) \times La_{melt}$). The shaded band on the $f_d = 0.74$ trajectory spans the constrained admissible defect radius ($r_0^{def} = 0.975$–0.993 Å; $D^{REE-H}(La) = 0.024$–0.137), indicating the range of maximum-f_d predictions consistent with the integrated geometric constraints. Symbols are paired melt-inclusion (MIZ) and host-zircon (ZRC) analyses from Gudelius et al. (2020), coloured by whether La_{zrc} lies above (red) or below (purple) the empirical threshold of $La_{zrc} = 0.1$ ppm proposed by Zou et al. (2019) (solid red line), above which zircon analyses are commonly interpreted as contaminated by micro-inclusions. Most Gudelius data fall along or below the lattice baseline, consistent with $f_d \approx 0$. However, the model predicts that under elevated defect-site fractions (e.g. hydrous, P-undersaturated systems) La_{zrc} can reach or exceed 0.1 ppm through structural, defect-coupled incorporation rather than micro-inclusion contamination, demonstrating that the Zou et al. (2019) threshold is not universally diagnostic but depends on melt composition and defect-site abundance. (For interpretation of the references to colour in this figure legend, the reader is referred to the web version of this article.) (For interpretation of the references to colour in this figure legend, the reader is referred to the web version of this article.)

in apparent La compatibility (Fig. 5a).

$$D_{tot}^{max}(La) = 0.26 \times 0.004 + 0.74 \times 0.121 = 0.091 \approx 0.09$$

The geological consequence is that La_{zrc} scales with both $D_{tot}(La)$ and La_{melt}. Fig. 5b therefore presents a family of trajectories in La_{zrc}–La_{melt} space rather than a single fixed cutoff, with the dry lattice prediction defining the low-f_d limit and increasing f_d shifting zircon La upward at constant melt composition.

For granitic melts with $La_{melt} \approx 50$–200 ppm, the mechanism could theoretically produce La_{zrc} up to several ppm. However, the mechanism is suppressed only where the zircon itself reaches $P_{mol} \approx REY_{mol}$, so that REE charge balance is carried by P rather than H^+ (as in the granitoid zircons of Meng et al., 2021); melt phosphorus saturation alone does not ensure this, since zircon crystallising even from apatite- or monazite-saturated melts can still incorporate excess REE balanced by H^+ (De Hoog et al., 2014; Section 5.2).

The key result is that the Zou et al. (2019) threshold corresponds approximately to the dry, lattice-dominated limit rather than to a universal boundary. In hydrous, P-undersaturated systems with elevated defect-site fractions, the REE^{3+}–H^+ mechanism can raise La_{zrc} above the dry-lattice prediction without requiring inclusions, whereas in dry or P-saturated systems the model collapses back toward the classical limit.

The exact La_{zrc} reached at a given La_{melt} depends on defect-site fraction, temperature, and uncertainty in defect-site geometry, so Fig. 5 should be interpreted as a physically bounded envelope rather than as a single deterministic cutoff.

4.3. The charge-balance proxy for f_d

Fig. 6 compares two independent estimates of the defect-site fraction: the charge-balance estimate $f_d^{CB} = (REY - P)/REY$ and the water-based estimate $f_d^{H_2O} = [H_2O]/([H_2O] + H_0)$. In the De Hoog system the two estimates correlate strongly ($r_s \approx 0.7$, $p < 0.001$), whereas granitoid zircons from Xia et al. (2021) show no meaningful correlation ($r_s = -0.13$, $p = 0.23$).

The physical reason is straightforward: in the De Hoog dataset, H^+ is the dominant charge-balancing mechanism for REE^{3+} not accommodated by P^{5+}, so charge-balance and water-content estimates of f_d recover the same underlying variable. In the Xia dataset, by contrast, total H_2O is decoupled from REE excess over P, indicating that the measured water is hosted largely by alternative defect populations rather than by the REE^{3+}–H^+ mechanism.

Fig. 6 is therefore a mechanistic validation figure rather than a calibration plot. Agreement between f_d^{CB} and $f_d^{H_2O}$ in De Hoog dataset demonstrates that the defect-site fraction is a measurable physical quantity where the mechanism is active, whereas their decoupling in Xia dataset identifies a regime in which the same model should not be applied. In that regime D(La) cannot be reliably predicted from either proxy: the water-based estimate overestimates the defect-site fraction because most of the water is not REE-coupled, while the charge-balance estimate cannot distinguish REE excess balanced by H^+ from excess balanced by other cations such as Al^{3+} or Fe^{3+}, and so also overestimates it unless H^+-coupling is independently confirmed (e.g. by FTIR).

5. Discussion

5.1. The long-standing problem of REE excess over P and competing charge-balance mechanisms

The observation that REE + Y (mol) systematically exceeds P (mol) in natural igneous zircons predates the present model by more than two decades. Hoskin and Schaltegger (2003) compiled extensive trace-element data for igneous zircon and noted explicitly that the xenotime substitution ($REE^{3+} + P^{5+} = Zr^{4+} + Si^{4+}$) could account for only part of the REE budget in most samples. They proposed interstitial Al^{3+} and Fe^{3+} as the most likely additional charge-balance mechanisms, calculating that ~380 ppm interstitial *Al* would be required to charge-balance all excess REE^{3+} in their Boggy Plain Zoned Pluton zircons. Such abundances far exceed the *Al* now measured in natural zircon – averaging ~1 ppm in metaluminous (I-type) and ~10 ppm in peraluminous (S-type) grains, and only rarely exceeding a few tens of ppm (Wang and Trail, 2019) – so interstitial *Al* can supply this balance only exceptionally. They also noted, presciently, that "hydrous species, play an essential role in REE and Y substitution," though they did not pursue this quantitatively. The H^+ mechanism documented by De Hoog et al. (2014) and modelled here is therefore not the only possible charge-balance pathway for excess REE^{3+}, and competing mechanisms constrain where the present model applies.

The critical distinction is compositional. In the Fe—Ti oxide gabbros of the Vema Fracture Zone, *Al*, Fe, Mg, and Nb are below or near SIMS detection limits, contributing less than 2% of the total charge balance

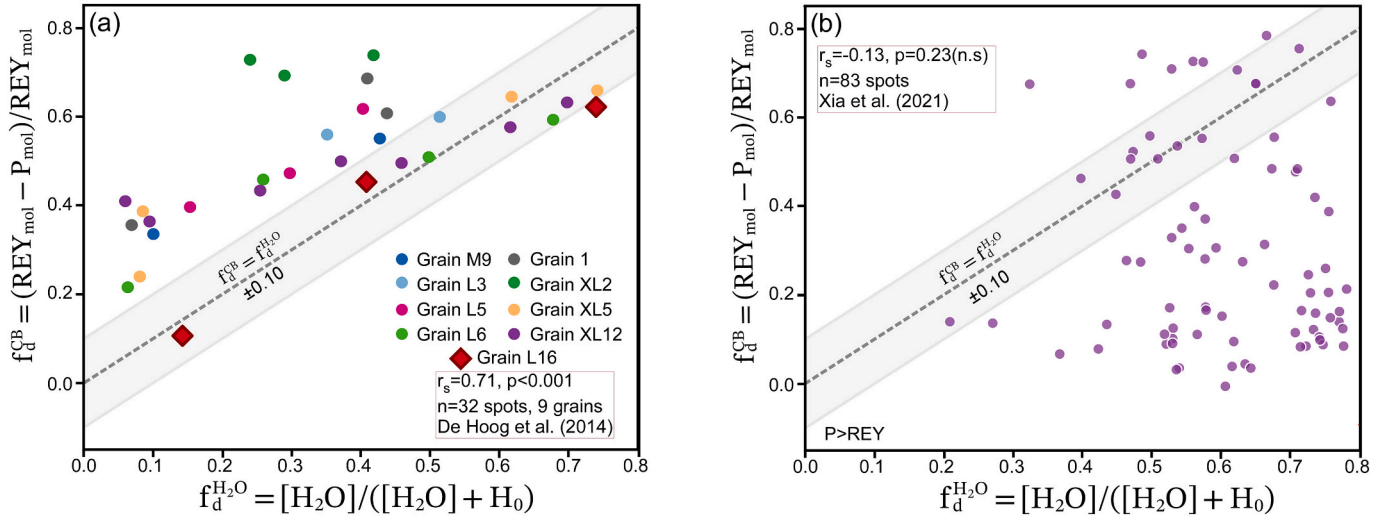


Fig. 6. Comparison of defect-site fraction estimated from water content and charge balance. (a) De Hoog et al. (2014) dataset (32 spots, 9 grains). The charge-balance estimate $f_d^{CB} = (REY_{mol} - P_{mol})/REY_{mol}$ is compared to the water-based estimate $f_d^{H_2O} = [H_2O]/([H_2O] + H_0)$ with $H_0 = 422$ ppm. The dashed line shows 1:1 correspondence and the shaded band indicates ±0.10. A strong positive correlation is observed ($r_s = 0.71$; $p < 0.001$). (b) Xia et al. (2021) dataset (83 filtered paired spots). The same comparison shows no significant correlation ($r_s = -0.13$; $p = 0.23$), reflecting decoupling between REY and P in systems where P exceeds REY.

(De Hoog et al., 2014). In such geochemically clean, mafic oceanic systems, H^+ emerges as the dominant additional charge-balance mechanism by default. In granitic systems – the dominant setting for most published zircon REE datasets - the situation is commonly reversed. P contents are higher – especially in S-type (peraluminous) suites, whose melts are P-rich (Burnham and Berry, 2017) – and often approach near-stoichiometric xenotime saturation, so excess REE^{3+} is increasingly charge-balanced by P^{5+} rather than by H^+; Al and Fe, though more variable in evolved melts, remain minor in most zircon (typically a few tens of ppm or less; Wang and Trail, 2019). The present model's calibration in an Al-poor, P-undersaturated oceanic gabbro system should not be extrapolated to granitic systems without first demonstrating that Al, Fe, and xenotime substitution are negligible, as the model cannot distinguish among these competing mechanisms from REE patterns alone.

This limitation is more severe than it might initially appear. Burnham and Berry (2012) explicitly note that their dry andesitic melt D values are "unsuitable for modelling REE behaviour in granitic systems owing to the expected theoretical dependence of D on temperature." By analogous reasoning, calibration of the H^+-coupled mechanism at 787 °C in an oceanic gabbro does not transfer directly to granitic systems crystallising at 650–750 °C with different melt structures and competing charge compensators. The three-criterion screening outlined above – P-undersaturation, sufficient $[H_2O]_{zrc}$, and absence of competing compensators - is a necessary but not sufficient set of conditions; independent FTIR confirmation remains the gold standard.

5.2. Reconciling experimental LREE partition coefficients with the H^+-coupled mechanism

One of the most persistent puzzles in zircon geochemistry is the systematic discrepancy between experimentally measured LREE partition coefficients and those derived from natural phenocryst–matrix pairs. Luo and Ayers (2009), working with hydrous peralkaline rhyolitic melts over 800–1300 °C, measured D(La) = 0.06–0.95 and D(Lu)/D(La) = 27–206, far less fractionated than the value of 706,522 for a natural zircon–dacite pair (Sano et al., 2002). They attributed this discrepancy to kinetic disequilibrium: rapid laboratory growth rates generated diffusive boundary layers enriched in incompatible LREE adjacent to the growing crystals, with Péclet numbers ~1.3 suggesting boundary-layer effects were active. Burnham and Berry (2012) disputed this interpretation for their dry andesitic experiments – their DREE patterns show much steeper La-to-Lu slopes (mean $\log(D_{Lu}/D_{La}) = 3.5$) more consistent with natural values - but agreed that kinetic effects could explain the shallower slopes in Luo and Ayers (2009).

The H^+-coupled mechanism offers a complementary explanation for elevated LREE in hydrous experiments that does not require invoking disequilibrium. The Luo and Ayers (2009) experiments used hydrous melts (~6 wt% H_2O added) and were conducted in the presence of monazite in 8 of 12 charges, providing both H^+ and P^{5+} as potential charge-balance mechanisms for REE^{3+} incorporation. If the mechanism is active in the laboratory as in nature, then at $[H_2O]_{melt} = 6$ wt%, the corresponding $[H_2O]_{zrc}$ could be 200–800 ppm (depending on the zircon–melt water partition coefficient), placing the system in the strongly detectable zone of our model. We emphasise, however, that there is no universal zircon–melt partition coefficient for water – it depends on the melt P_2O_5 and REE content (De Hoog et al., 2014) - and that not all of this zircon H need be REE-coupled, since Si- and Zr-vacancy substitutions also incorporate hydrogen (Cui et al., 2023; Section 5.6); the 200–800 ppm range is therefore indicative rather than a firm prediction. The elevated D(La) values reported by Luo and Ayers (2009) - up to 0.95 - substantially exceed even our maximum model prediction (~0.1 at maximum f_d), which might suggest that kinetic boundary-layer enrichment contributed in addition to the H^+ mechanism. Distinguishing the relative contributions of these two processes would require re-running the Luo and Ayers (2009) experiments with simultaneous SIMS measurement of $[H_2O]$ in the run-product zircon - precisely the experimental design identified as the priority for future work in Section 5.7.

In contrast, the Burnham and Berry (2012) dry experiment, which produced D(La) = 0.002 consistent with lattice-strain-only predictions, anchors the zero-water end of the continuum. The factor-of-50 difference in D(La) between Burnham and Berry (dry) and Thomas et al. (2002; hydrous, P-free; D(La) median ~ 0.05) points directly to the H^+-coupled mechanism as the most likely explanation for the hydrous enhancement, given that P is below detection limits in the Thomas et al. zircon dataset and kinetic effects are less likely in slowly growing natural crystals. Our model correctly identifies this as a region where the mechanism should be active (temperature ~ 940 °C, melt H_2O = 4–9 wt %), though the large scatter in Thomas et al. partition coefficients (IQR ~1 order of magnitude per element) prevents a quantitative test.

5.3. The charge-balance approach versus REE pattern shape: what each tells us

De Hoog et al. (2014) demonstrated that charge balance closure – $(H + P)/REY \approx 1$ on an atomic basis - provides the most direct evidence for the coupled H^+–REE^{3+} mechanism. In 31 of 32 Vema spots, $P_{mol} < REY_{mol}$, and $H_{mol} \approx REY_{mol} - P_{mol}$, establishing a near-perfect stoichiometric relationship. The charge-balance proxy f_d^{CB} used here extends this approach by converting the REE excess fraction into a fractional site occupancy that is directly comparable with the model output.

The coupled-substitution framework on which this competition rests is independently supported by experiment. Grant and Wood (2010), in olivine synthesis experiments at fixed melt composition, isolated the charge-coupled mechanisms by which 1+ and 3+ cations are incorporated into a silicate lattice, establishing that such mechanisms are resolvable only when compositional variables other than the trace elements themselves are held constant. For zircon, Shang et al. (2024) experimentally showed that phosphorus abundance exerts opposite controls on the zircon–melt partition coefficients of Al^{3+} and Li^+ while leaving most other trace elements unaffected; because Al^{3+} and Li^+ are the cations whose uptake is most directly tied to local charge balance, this is direct evidence that P availability governs the charge-compensation of aliovalent cations on the Zr^{4+} site – the xenotime-type accounting ($REE^{3+} + P^{5+} \rightleftharpoons Zr^{4+} + Si^{4+}$) that, in competition with H^+, controls REE^{3+} incorporation in the present model.

In the De Hoog dataset, f_d^{CB} and independent water-based estimates of f_d correlate, demonstrating that charge balance and water content recover the same underlying variable where the REE^{3+}–H^+ mechanism is active. The model therefore does not receive independent validation from Nd/Lu alone; rather, it provides the quantitative translation between charge-balance language, water-content language, and REE-pattern language, showing that all three converge on the same physical quantity: the fraction of Zr sites occupied by REE^{3+}–H^+ pairs.

Recent single-crystal compressibility work on zircon (Maitani et al., 2025) shows that the elastic term in lattice-strain formulations is better represented by local Zr—O bond compressibility rather than by Poisson-solid estimates derived from site bulk modulus. Bond-scale moduli (e.g., ~412–789 GPa for distinct Zr—O bonds) reproduce zircon–melt partitioning more accurately than lower values inferred from polyhedral compressibility, highlighting the strongly anisotropic and local nature of elastic response at the substitution site. This supports the treatment of E in the present defect-modified model as a local structural property of the substitution environment, rather than a bulk or polyhedral average, and reinforces the physical basis for distinguishing lattice and defect-site elastic parameters.

The two approaches have complementary strengths. The charge-balance diagnostic requires P to be measured at high precision alongside REY, which is routine in SIMS but less reliable in LA-ICP-MS. Phosphorus is monoisotopic (^{31}P), and that single mass is subject to isobaric interference both in the background and during ablation;

combined with the low ionization efficiency of phosphorus in an Ar plasma and the typically low P concentrations in oceanic gabbro zircons, this limits the precision attainable by LA-ICP-MS. The Nd/Lu ratio, by contrast, is measurable with excellent precision in routine LA-ICP-MS without any additional elements, making it the more practical tool for applying the model to archived datasets. Streicher et al. (2023) noted that LREE in zircon are generally poorly constrained in both experimental and natural datasets due to their low concentrations and susceptibility to inclusion contamination - a caveat that applies to La and, to a lesser extent, Ce and Pr. Nd and Lu are analytically more robust, which is why Nd/Lu rather than La/Lu or Ce*/Lu is the primary observable of the model.

5.4. The temperature–H_2O detection threshold in context of published datasets

The detection threshold map (Fig. 4) can be used to interpret the null results reported in published literature. Meng et al. (2021), studying hydrous granitoids from southern Tibet with zircon $[H_2O] = 58–920$ ppm, reported no significant H_2O–Nd/Lu correlation. Our model correctly predicts this: the Meng et al. samples have $P_{mol} > REY_{mol}$ in the majority of analyses, placing $f_d^{CB} \leq 0$ and making the H^+ pathway unavailable regardless of $[H_2O]$. This is a mechanism-specific null result, confirming that the absence of a Nd/Lu signal should not be interpreted as an absence of structural water in zircon - the water may be present but coupled to Si- or Zr-vacancy mechanisms rather than to REE substitution.

Xia et al. (2021), studying Gangdese granitoids, found $[H_2O]_{zrc}$ up to 2339 ppm but also no H_2O–REE correlation. The reason differs from that in the Meng et al. dataset; Xia et al. identified a strong correlation between $[H_2O]$ and Hf content (a proxy for magma evolution and cooling), which means $[H_2O]$ and temperature co-vary systematically across grains. Higher $[H_2O]$ grains are also lower-temperature grains with higher D values for all REE; the temperature effect on D_0^{REE-P} thus partially mimics and partially cancels the defect-site effect, making the net REE pattern signal uninterpretable. This illustrates an inherent ambiguity of the approach, arising from the temperature dependence of the Nd/Lu signal (Section 4.1): where $[H_2O]$ and temperature co-vary, as they commonly do in granitic systems during prolonged crystallisation, the model cannot uniquely recover f_d from REE patterns alone without independent temperature constraints.

Gudelius et al. (2020) provide an instructive contrast. Their Bushveld Complex zircons crystallised from melts with $H_2O = 1.6–4.0$ wt% (measured directly in melt inclusions), comparable to the Thomas et al. (2002) system, yet $D(La) = 0.003$ in their felsic samples — essentially the lattice-only prediction of Burnham and Berry (2012), with no MREE enrichment. Their zircons were not analysed for water, so they cannot be placed on the detection-threshold map directly; instead they are diagnostic through their REE systematics. Although these zircons carry a substantial rare-earth excess over phosphorus ($P_{mol}/REY_{mol} = 0.08–0.49$, median 0.16, so xenotime substitution accommodates only ~16% of the rare-earth budget on average), their REE patterns remain lattice-like ($f_d \approx 0$). The defect signal is thus absent despite both appreciable melt water and a large charge-balance excess. This indicates that the excess REE^{3+} is compensated by a mechanism other than H^+ — in granitic zircon most plausibly interstitial Al^{3+} (Hoskin and Schaltegger, 2003), although *Al* was not determined in the Gudelius zircons. These zircons therefore exemplify the regime, analogous to the Xia et al. (2021) dataset (Section 4.3), in which a charge-balance excess exists but the H^+-coupled mechanism is inactive, so the model does not apply. The contrast between De Hoog (mechanism active, signal present), Thomas (mechanism expected but signal unresolvable due to data quality), and Gudelius (mechanism inactive despite high melt water) illustrates both the utility and the limits of the framework as a pre-screening tool.

5.5. The REE^{3+}–H^+ mechanism and the Zou et al. (2019) La threshold

Zou et al. (2019) proposed La ≤ 0.1 ppm as an empirical criterion for identifying inclusion-free zircon, based on 7626 natural zircon analyses from the GEOROC database. Their argument rested implicitly on the dry lattice-strain model: $D_{REE-P}(La) \approx 0.004$ at typical igneous temperatures, so even at $La_{melt} = 25$ ppm only 0.1 ppm La should enter the lattice. Any La above this was attributed to sub-micron inclusions of La-rich phases (monazite, allanite, apatite).

The present model refines this picture by showing that La_{zrc} depends on both melt composition and defect-site occupancy. At low f_d the system collapses to the classical lattice-strain limit, whereas increasing f_d progressively elevates $D_{tot}(La)$ and can raise La_{zrc} above the dry-lattice prediction without requiring inclusions (Fig. 5). The relevant test is therefore not a single fixed ppm threshold, but whether an observed La_{zrc} is consistent with the combination of La_{melt} and a plausible defect-site fraction for the system of interest.

The Zou threshold is therefore not a universal inclusion-free criterion; it is an approximation valid specifically for dry or P-saturated systems where $D_{tot}(La) \approx D_{REE-P}(La)$. In hydrous, P-undersaturated melts it can be exceeded by lattice-bound La, and misidentifying such grains as contaminated would discard geochemically meaningful data. A physically grounded criterion would instead test whether the observed La_{zrc} is consistent with $D_{tot}(La, T, [H_2O]) \times La_{melt}$, which requires knowledge of temperature, water content, and melt La concentration. Where these are available, the Zou threshold should be replaced by this system-specific test.

For typical MORB-affinity or depleted granitic melts ($La_{melt} < 1$ ppm), the Zou threshold remains a conservative practical guide. For enriched granitic, alkalic, or carbonatitic systems with $La_{melt} > 2$ ppm, the threshold becomes unreliable even at modest f_d, and the REE^{3+}–H^+ mechanism cannot be ruled out as a source of La > 0.1 ppm in genuinely inclusion-free grains.

5.6. Implications for quantitative water reconstruction from zircon REE

The charge-balance approach of De Hoog et al. (2014) established that zircon water content cannot be simply used to reconstruct melt $[H_2O]$ without knowledge of P and REE in the melt, because the equilibrium partitioning of H, P, and REE into zircon is interdependent. The present model formalises this interdependence: $f_d = [H_2O]_{REE}/([H_2O]_{REE} + H_0)$, where $[H_2O]_{REE}$ is the component specifically coupled to REE^{3+} rather than total structural water.

Cui et al. (2023) extended this picture further, demonstrating on ten natural megacrystic zircons that in most samples >62% of total $[H_2O]$ is accounted for by Si-vacancy (3385/3420 cm^{-1}) and Zr-vacancy (3200 cm^{-1}) substitutions, independent of REE. This has a direct bearing on the applicability of Eq. (7): where vacancy mechanisms dominate, $[H_2O]_{total}$ substantially exceeds $[H_2O]_{REE}$, and using total $[H_2O]$ as input to the Langmuir function overestimates f_d. Strikingly, the Vema gabbro zircons studied by De Hoog et al. (2014) showed the opposite behaviour – the 3100 cm^{-1} band dominated, 3385/3420 cm^{-1} bands were absent, and $[H_2O]_{REE} \approx [H_2O]_{total}$ - precisely the conditions required for Eq. (7) to be valid without correction. Following De Hoog et al. (2014), this likely reflects the high silica activity of the evolved, zircon-saturated gabbroic system, which suppresses the Si-vacancy (hydrogrossular) substitution; that mechanism is favoured instead at low silica activity, as in kimberlites and in olivine. High-aSiO_2 granitic melts likewise suppress hydrogrossular, so correction is needed there not because of Si vacancies but because of the REE-independent Zr-vacancy substitution ($Zr^{4+} = 4H^+$; the 3200 cm^{-1} band of Cui et al., 2023), which is not governed by silica activity, and because of radiation-damage water in older grains – both of which raise $[H_2O]_{total}$ above $[H_2O]_{REE}$.

Trail et al. (2011) synthesised Lu-doped hydrous zircon and found that undoped zircon contained ~188 ppm H_2O (at 1650 °C) from hydrogrossular substitution alone - a baseline that the REE-doped

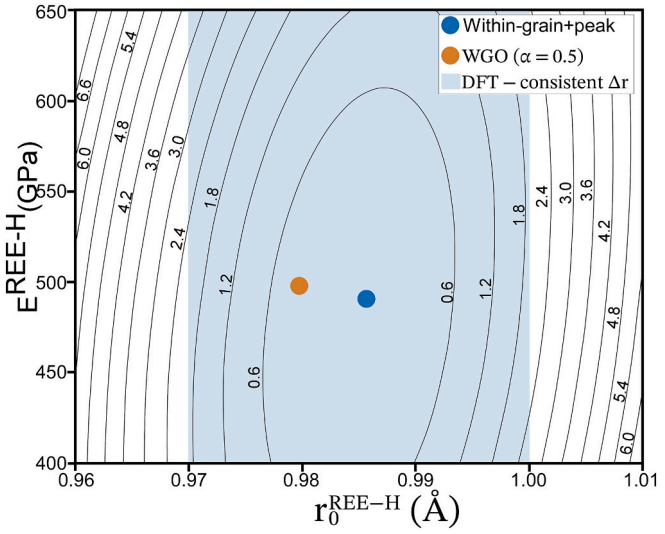


Fig. 7. Identifiability and integrated constraints on defect-site parameters. Contours map the Nd/Lu misfit over the defect-site optimal radius r_0^{REE-H} and elastic modulus E^{REE-H}, revealing an elongated minimum, a family of solutions that produce comparable fits to the De Hoog dataset. Contour labels give the Nd/Lu misfit minimised in the grid search (lower values indicate a better fit), drawn at intervals of 0.6. Points indicate independently derived solutions from weighted global optimisation (WGO; $\alpha = 0.5$) and within-grain + peak-constrained inversion. The shaded band represents the range of modest site expansion consistent with first-principles studies of REE–H defects in zircon. For reference, the dry REE–P site lies at $r_0^{REE-P} = 0.9445$ Å and $E^{REE-P} = 517$ GPa, to the left of the plotted radius range, so the REE–H site is both expanded in optimal radius and elastically softer than the REE–P site, as expected for a hydrous, charge-compensated substitution. The convergence of these independent constraints restricts the admissible solution space to a narrow region near $r_0^{REE-H} \approx 0.98$–0.99 Å, demonstrating that the defect-site radius is well constrained while the residual uncertainty lies chiefly in E^{REE-H}, which the Nd/Lu ratio constrains only weakly.

mechanism sits on top of, not instead of. This baseline hydrogrossular contribution, parameterised by Balan et al. (2013) as the dominant mechanism for crystalline (non-metamict) zircons, implies that any attempt to use $[H_2O]_{total}$ to estimate f_d must account for the hydrogrossular background before interpreting the remainder as REE-coupled. In the De Hoog calibration zircons this background was negligible - their spectra are dominated by the 3100 cm^{-1} (REE-coupled) band with the hydrogrossular bands essentially absent, so $[H_2O]_{total} \approx [H_2O]_{REE}$; in zircons where hydrogrossular OH is significant the correction would be substantially larger.

5.7. *Outstanding requirement: experimental calibration across temperature and composition*

Streicher et al. (2023) systematically compiled zircon–melt D_{REE} values across 39 datasets and established the r_0–E constraint and D_0 temperature dependence adopted for the lattice site parameters in this study. A key conclusion of Streicher et al. is that the temperature dependence of D_0^{REE-P} is well-established but that no systematic pressure dependence is apparent from available data. Critically, they also noted that LREE are poorly constrained in virtually all datasets – the very quantities that are most sensitive to the defect-site mechanism - due to their low concentrations and analytical detection challenges. Our initial unconstrained Nd/Lu optimum yields $D_0^{REE-H} = 344.5$, but the weighted global optimisation and within-grain inversions show that the main persistent uncertainty is not simple lack of signal but covariance between r_0^{REE-H} and E_{REE-H} (Fig. 7). The existing data constrain the defect-related enrichment to be centred in MREE radius space, yet the exact La-side tail remains weakly resolved because La, Ce, and Pr are the least precisely determined elements.

This situation is unlikely to improve without purpose-designed experiments in which: (a) the full REE suite from La to Lu is measured in both zircon and coexisting melt; (b) melt $[H_2O]$ is systematically varied from 0 to >5 wt% in a single, controlled compositional series; and (c) $[H_2O]$ in the run-product zircon is measured directly by SIMS or FTIR. None of the three available experimental datasets – Burnham and Berry (2012), Rubatto and Hermann (2007), Luo and Ayers (2009) - satisfies all three criteria simultaneously. Until such a dataset exists, r_0^{REE-H} will remain empirical and partially model-dependent. The present dataset robustly calibrates Nd/Lu and the general MREE-centred geometry of the defect site, but absolute LREE predictions should still be regarded as semi-quantitative rather than precision estimates.

6. Conclusions

We present the first physically grounded, calibrated two-population lattice strain model for the REE^{3+}–H^+ coupled incorporation mechanism in zircon. The principal findings are as follows.

1. The bulk partition coefficient is expressed as a weighted sum of contributions from the ideal ZrO_8 site and a defect site that is only modestly enlarged relative to the ideal ZrO_8 site. Initial Nd/Lu calibration gives $r_0^{REE-H} = 0.9916$ Å, $E_{REE-H} = 592.1$ GPa, and $D_0^{REE-H} = 344.5$, whereas combined weighted global optimisation, within-grain REE-pattern inversion, and DFT-consistent site expansion favour an effective radius near $r_0^{REE-H} \approx 0.984$ Å with an admissible envelope of approximately 0.975–0.993 Å. The physically constrained defect-site parameters used in Figs. 2 and 3 and Table S1 – $r_0 = 0.9857$ Å, $E = 490.1$ GPa, and $D_0 = 40.58$ – lie within this envelope; their lower E and D_0 relative to the unconstrained fit reflect the r_0–E–D_0 trade-off (Section 3.3), under which many parameter combinations reproduce the Nd/Lu data. The model reduces exactly to the classical single-parabola formulation when $f_d = 0$.
2. Calibration of defect-site parameters against 32 SIMS spots from Vema Fracture Zone gabbro zircons gives RMSE = 0.154 $\log_{10}$ units with no systematic offset between predicted and observed Nd/Lu. The within-grain $[H_2O]$–Nd/Lu covariation in grain L16 (17-fold $[H_2O]$ decrease, 5-fold Nd/Lu decrease, flat Yb/Lu) constitutes causal evidence for the mechanism with Nd/Lu tracking $[H_2O]$ rather than the covarying temperature. Supplementary within-grain pattern-shape constraints further show that the defect-related enrichment is centred in the Nd–Sm–Gd region, explaining why Nd/Lu is the most robust primary observable of the model.
3. A quantitative detection threshold in temperature–$[H_2O]$ space defines the conditions under which the REE^{3+}–H^+ signal in Nd/Lu is resolvable above geological noise. Two published systems (De Hoog et al. (2014), above threshold; Thomas et al. (2002), above threshold but unresolvable due to absent zircon H_2O) fall where the model predicts, whereas the Gudelius et al. (2020) granitic zircons exemplify a contrasting regime in which the H^+-coupled mechanism is inactive — their REE patterns remain lattice-like despite melt water comparable to systems where the mechanism operates.
4. The REE^{3+}–H^+ mechanism can produce $La_{zrc} > 0.1$ ppm through genuine lattice incorporation in hydrous, P-undersaturated systems. The model predicts that the REE^{3+}–H^+ mechanism can elevate La above classical lattice-strain predictions under sufficiently high defect-site occupancy, demonstrating that the empirical threshold of Zou et al. (2019) reflects a low-f_d limit rather than a universal indicator of inclusion contamination. The Zou et al. (2019) La ≤ 0.1 ppm threshold is therefore not a universal inclusion-free criterion; it is a valid approximation specifically for dry or P-saturated systems where $D_{tot}(La) \approx D_{REE-P}(La)$. In hydrous P-undersaturated melts it can be exceeded by lattice-bound La. A physically grounded criterion

requires testing whether observed La_{zrc} is consistent with $D_{tot}(La, T, [H_2O]) \times La_{melt}$ rather than applying a fixed ppm threshold.

5. The charge-balance proxy $f_d^{CB} = (REY - P)/REY$, recoverable from standard LA-ICP-MS data, provides an estimate of defect-site occupancy that correlates with water-based estimates where the REE^{3+}-H^+ mechanism is active. However, f_d^{CB} assumes that P^{5+} and H^+ are the only significant charge compensators. Where a third mechanism operates, as in the Gudelius et al. (2020) zircons where it is inferred to be interstitial Al^{3+}, f_d^{CB}overestimates the H-coupled fraction, and at present this can be recognised only from the lattice-like shape of the REE pattern. Until the conditions controlling such competing mechanisms are established, forward modelling of REE partitioning requires either independent confirmation of H^+ coupling (e.g. by FTIR) or measurement of competing compensators such as Al.
6. The calibration is based on a single natural dataset (De Hoog et al., 2014), in which melt composition, a_{TiO_2}, a_{SiO_2} and a_{H_2O} are not independently constrained; calibrating on intra-zircon Nd/Lu, together with the fixed-melt L16 transect, mitigates but does not remove this limitation. Experimental calibration, and additional natural zircons with measured H, P and Al, are required to test the model beyond this system.

The model is applicable specifically to P-undersaturated, hydrous, low-temperature magmatic zircons confirmed free of competing charge compensators - conditions met in oceanic lower-crustal systems such as the Vema gabbros, but not where xenotime substitution dominates the REE charge balance, most notably in the P-rich S-type (peraluminous) granites (Burnham and Berry, 2017). The central quantitative result - that H^+-coupled incorporation saturates below the Zou et al. (2019) inclusion-free threshold in typical melts - clarifies the interpretation of LREE anomalies in natural zircon and defines where the mechanism is, and is not, a plausible explanation for observed concentrations.

CRediT authorship contribution statement

Ioan V. Sanislav: Writing – original draft, Visualization, Validation, Methodology, Investigation, Formal analysis, Data curation, Conceptualization. **Mabrouk Sami:** Writing – review & editing, Investigation, Formal analysis, Conceptualization.

Declaration of competing interest

The authors declare that they have no known competing financial interests or personal relationships that could have appeared to influence the work reported in this paper.

Acknowledgements

IVS would like to acknowledge support from EGRU and James Cook University whereas MS would like to acknowledge support from United Arab Emirates University.

Appendix A. Supplementary data

Supplementary data to this article can be found online at https://doi.org/10.1016/j.chemgeo.2026.123802.

Data availability

All data used in the preparation of this manuscript was sourced from published journal articles available for download from the publisher and cited appropriately in the manuscript text.

References

Balan, E., Yii, H., Blanchard, M., 2013. First-principles study of OH-defects in zircon. Phys. Chem. Miner. 40, 547–554.
Blundy, J., Wood, B., 1994. Prediction of crystal-melt partition coefficients from elastic moduli. Nature 372, 452–454.
Brice, J.C., 1975. Some thermodynamic aspects of the growth of strained crystals. J. Cryst. Growth 28, 249–253.
Burnham, A.D., Berry, A.J., 2012. An experimental study of trace element partitioning between zircon and melt as a function of oxygen fugacity. Geochim. Cosmochim. Acta 95, 196–212.
Burnham, A.D., Berry, A.J., 2017. Formation of Hadean granites by melting of igneous crust. Nat. Geosci. 10, 457–461.
Cui, Z., Xia, X.-P., Spencer, C.J., Hui, H., Yang, Q., Zhang, W.-F., Zhang, L., Xu, Y., Xu, J., Lai, C.-K., Zhang, Y., 2023. Incorporation of hydrogen into zircon through multi-coupling mechanisms and its geochemical implications. Lithos 446–447, 107127.
De Hoog, J.C.M., Lissenberg, C.J., Brooker, R.A., Hinton, R., Trail, D., Hellebrand, E., EIMF, 2014. Hydrogen incorporation and charge balance in natural zircon. Geochim. Cosmochim. Acta 141, 472–486.
Ferry, J.M., Watson, E.B., 2007. New thermodynamic models and revised calibrations for the Ti-in-zircon and Zr-in-rutile thermometers. Contrib. Mineral. Petrol. 154, 429–437.
Grant, K.J., Wood, B.J., 2010. Experimental study of the incorporation of Li, Sc, Al and other trace elements into olivine. Geochim. Cosmochim. Acta 74, 2412–2428.
Gudelius, D., Zeh, A., Almeev, R.R., Wilson, A.H., Fischer, L.A., Schmitt, A.K., 2020. Zircon melt inclusions in mafic and felsic rocks of the Bushveld Complex – Constraints for zircon crystallization temperatures and partition coefficients. Geochim. Cosmochim. Acta 289, 158–181.
Hoskin, P.W.O., Schaltegger, U., 2003. The composition of zircon and igneous and metamorphic petrogenesis. Rev. Mineral. Geochem. 53, 27–62.
Luo, Y., Ayers, J.C., 2009. Experimental measurements of zircon/melt trace-element partition coefficients. Geochim. Cosmochim. Acta 73, 3656–3679.
Maitani, S., Sinmyo, R., Higuchi, H., Ikeda-Fukazawa, T., Kawaguchi-Imada, S., 2025. Compressibility of single-crystal zircon up to 19 GPa: implications for the partitioning coefficient of trace elements. Eur. J. Mineral. 37, 257–267. https://doi.org/10.5194/ejm-37-257-2025.
McDonough, W.F., Sun, S.-S., 1995. The composition of the Earth. Chem. Geol. 120, 223–253.
Meng, J., Xia, X., Ma, L., Jiang, Z., Xu, J., Cui, Z., Yang, Q., Zhang, W., Zhang, L., 2021. A H_2O-in-zircon perspective on the heterogeneous water content of crust-derived magmas in southern Tibet. Sci. China Earth Sci. 64, 1184–1194.
Piazolo, S., La Fontaine, A., Trimby, P., Harley, S., Yang, L., Armstrong, R., Cairney, J.M., 2016. Deformation-induced trace element redistribution in zircon revealed using atom probe tomography. Nat. Commun. 7, 10490.
Rubatto, D., Hermann, J., 2007. Experimental zircon/melt and zircon/garnet trace element partitioning and implications for the geochronology of crustal rocks. Chem. Geol. 241, 38–61.
Sano, Y., Terada, K., Fukuoka, T., 2002. High mass resolution ion microprobe analysis of rare earth elements in silicate glass, apatite and zircon: lack of matrix dependency. Chem. Geol. 184, 217–230.
Shang, S., Lin, Y., van Westrenen, W., Brouwer, F.M., 2024. Evolution of magma compositions and phosphorus availability in early Earth's crust: New constraints from zircon-melt partitioning experiments. Geology 52, 794–798.
Shannon, R.D., 1976. Revised effective ionic radii and systematic studies of interatomic distances in halides and chalcogenides. Acta Crystallogr. A32, 751–767.
Stolper, E., 1982. The speciation of water in silicate melts. Geochim. Cosmochim. Acta 46, 2609–2620.
Streicher, L.B., van Westrenen, W., Hanchar, J.M., Brouwer, F.M., 2023. A REE-based zircon geothermometer based on improved lattice strain modeling of zircon-melt REE partition coefficients. Geochim. Cosmochim. Acta 346, 54–64.
Thomas, J.B., Bodnar, R.J., Shimizu, N., Sinha, A.K., 2002. Determination of zircon/melt trace element partition coefficients from SIMS analysis of melt inclusions in zircon. Geochim. Cosmochim. Acta 66, 2887–2901.
Trail, D., Thomas, J.B., Watson, E.B., 2011. The incorporation of hydroxyl into zircon. Am. Mineral. 96, 60–67.
Trail, D., Watson, E.B., Tailby, N.D., 2012. Ce and Eu anomalies in zircon as proxies for the oxidation state of magmas. Geochim. Cosmochim. Acta 97, 70–87.
Wang, Y., Trail, D., 2019. Aluminum partitioning between zircon and haplogranitic melts: the influence of temperature and melt composition. Chem. Geol. 511, 71–80.
Watson, E.B., Harrison, T.M., 1983. Zircon saturation revisited: temperature and composition effects in a variety of crustal magma types. Earth Planet. Sci. Lett. 64, 295–304.
Watson, E.B., Wark, D.A., Thomas, J.B., 2006. Crystallization thermometers for zircon and rutile. Contrib. Mineral. Petrol. 151, 413–433.
Wood, B.J., Blundy, J.D., 1997. A predictive model for rare earth element partitioning between clinopyroxene and anhydrous silicate melt. Contrib. Mineral. Petrol. 129, 166–181.
Xia, X.P., Meng, J.T., Ma, L., Spencer, C.J., Cui, Z.X., Zhang, W.F., Yang, Q., Zhang, L., 2021. Tracing magma water evolution by H 2 O-in-zircon: A case study in the Gangdese batholith in Tibet. Lithos 404, 106445.
Zou, X., Qin, K., Han, X., Li, G., Evans, N.J., Li, Z., Yang, W., 2019. Insight into zircon REE oxy-barometers: a lattice strain model perspective. Earth Planet. Sci. Lett. 506, 87–96.